Contributions to Mineralogy and Petrology (2019) 174:32
https://doi.org/10.1007/s00410-019-1570-x

ORIGINAL PAPER

Decadal transition from quiescence to supereruption: petrologic investigation of the Lava Creek Tuff, Yellowstone Caldera, WY

Hannah I. Shamloo[1] · **Christy B. Till**[1]

Received: 19 October 2018 / Accepted: 5 April 2019

Abstract

The magmatic processes responsible for triggering nature's most destructive eruptions and their associated timescales remain poorly understood. Yellowstone Caldera is a large silicic volcanic system that has had three supereruptions in its 2.1-Ma history, the most recent of which produced the Lava Creek Tuff (LCT) ca. 631 ka. Here we present a petrologic study of the phenocrysts, specifically feldspar and quartz, in LCT ash in order to investigate the timing and potential trigger leading to the LCT eruption. The LCT phenocrysts have resorbed cores, with crystal rims that record slightly elevated temperatures and enrichments in magmaphile elements, such as Ba and Sr in sanidine and Ti in quartz, compared to their crystal cores. Chemical data in conjunction with mineral thermometry, geobarometry, and rhyolite-MELTS modeling suggest the chemical signatures observed in crystal rims were most likely created by the injection of more juvenile silicic magma into the LCT sub-volcanic reservoir, followed by decompression-driven crystal growth. Geothermometry and barometry suggest post-rejuvenation, pre-eruptive temperatures and pressures of 790–815 °C and 80–150 MPa for the LCT magma source. Diffusion modeling utilizing Ba and Sr in sanidine and Ti in quartz in conjunction with crystal growth rates yield conservative estimates of decades to years between rejuvenation and eruption. Thus, we propose rejuvenation as the most likely mechanism to produce the overpressure required to trigger the LCT supereruption in less than a decade.

Keywords Yellowstone · Supereruption · Feldspar-liquid thermometry · TitaniQ · Rhyolite-MELTS · Diffusion chronometry · Sanidine · Quartz

Introduction

Supereruptions, eruptions that produce volcanic products of > 1000 km^3 (Sparks 2005), represent an extreme end-member in volcanic eruption style and have the potential to devastate human populations globally. Despite the threat associated with these high-risk events, the processes responsible for mobilizing large amounts of silicic magma are poorly understood. Improving our knowledge of supereruption pre-eruptive processes requires an understanding of the physical mechanisms responsible for triggering past eruptions, as well as the timescales associated with specific triggers.

In recent decades, two end-member models have emerged to explain the mechanism by which a magma achieves the overpressure necessary to drive an eruption: rejuvenation and volatile exsolution. In the first model hot, lower-viscosity, crystal-poor melt batches interact with a cooler, more evolved, and more crystalline "mush" with varying degrees of melt, a process commonly referred to as rejuvenation (Cashman and Sparks 2013; Bachmann and Huber 2016). For smaller scale eruptions, diffusion chronometry timescales associated with these rejuvenation events are on the order of thousands of years but can be as short as decades (e.g., Hawkesworth et al. 2004; Turner and Costa 2007 and citations within; Costa et al. 2011; Till et al. 2015). The second end-member model for achieving overpressure involves volatile exsolution prior to or during magma ascent driven by decompression (i.e., "first boiling" Sisson and Bacon 1999) or driven by the crystallization of anhydrous phases (i.e., "second boiling" Sisson and Bacon 1999). For

Communicated by Timothy L. Grove.

Electronic supplementary material The online version of this article (https://doi.org/10.1007/s00410-019-1570-x) contains supplementary material, which is available to authorized users.

✉ Hannah I. Shamloo
hshamloo@asu.edu

[1] School of Earth and Space Exploration, Arizona State University, 781 Terrace Mall, Tempe, Arizona 85287, USA

Published online: 19 April 2019

example, second boiling has been invoked for sustaining a Plinian column during the formation of the Bishop Tuff (Wallace et al. 1995). Although, these two models need not be mutually exclusive and are not the only mechanisms that trigger eruptions. However, we consider these end members of internal magma body eruption triggers for the purposes of this study, as other internal triggers are derivatives of these two models.

In addition to internal eruption triggers, there are external triggering mechanisms such as magma buoyancy. While thermomechanical modeling suggests magma buoyancy alone cannot provide sufficient overpressure to trigger an eruption (< 0.1 MPa; Gregg et al. 2015), it can play an important role in the lead up to an eruption during the rapid assembly of multiple melt pockets, as has been suggested for the Bishop Tuff (e.g., Gualda and Sutton 2016). Other external triggers have been investigated including tectonic stress and magma roof stability (Allan et al. 2012; Cabaniss et al. 2018; Gregg et al. 2015), although, thus far these processes remain difficult to trace in the rock record due to the lack of simultaneous geophysical and geodetic monitoring data.

Supereruptions have paved the path of calderas known as the Yellowstone-Snake River Plain of the western United States. The present manifestation of this continental hotspot, the Yellowstone caldera, has produced three supereruptions over the last ~ 2.1 m.y., including the Huckleberry Ridge Tuff, Mesa Falls Tuff, and most recently, Lava Creek Tuff (LCT). The LCT eruption dispersed ash over the greater United States (Fig. 1a, inset), representing a natural laboratory for understanding the processes and timescales leading to supereruptions. Understanding the lead up to the LCT eruption is also of great interest to both scientists and the general public due to Yellowstone's location in the central United States, its on-going hydrothermal and earthquake activity, and its destructive past. This study combines in situ geochemistry via Electron Probe Micro-Analyzer and high-spatial resolution Nano-scale Secondary Ion Mass Spectrometry, diffusion chronometry, feldspar-liquid thermometry, TitaniQ thermometry, geobarometry, and petrologic phase equilibria modeling to conduct a holistic, multi-phase investigation of the events and possible eruption trigger of the LCT.

Previous studies of the LCT

Yellowstone's most recent caldera forming eruption is traditionally thought to have produced two members, LCT-A and LCT-B, which represent two eruptive phases indistinguishable in age but separated by a cooling break (Gansecki 1998; Gansecki et al. 1998; Christiansen 2001; Matthews et al. 2015; Wotzlaw et al. 2015; Jicha et al. 2016; Mark et al. 2017). A recent study, combining field and geochronology observations, suggests that LCT may have two additional tuff units that precede both members A and B; however, their relative volumes remain unknown (Wilson et al. 2018). LCT-A and -B are approximately equal in volume (~ 500 km^3) with the ash from the earlier erupted LCT-A covering a more limited region relative to LCT-B (Fig. 1a). LCT deposits including ignimbrite and ash are distributed around Yellowstone caldera and their isopach distributions suggest each member (A and B) erupted from separate caldera ring fracture vents (Christiansen 2001). Stratigraphically, members A and B are separated by a layer of fallout ash from the beginning of the eruption of LCT-B (Fig. 1c), the affinity of which is known by the absence of amphibole found exclusively in LCT-A. Phenocrysts of sanidine, quartz, and minor amounts of magnetite, ilmenite, fayalite, and zircon characterize the minerology of LCT-A and -B, with the addition of amphibole in LCT-A (Hildreth 1981, Christiansen 2001). LCT-B fallout ash is the focus of this study, as fallout ash quenches quickly serving as a better window into the magmatic processes prior to the eruption.

Recent $^{40}Ar/^{39}Ar$ dating of individual LCT-B sanidine yield LCT eruption ages of 631 ± 4 ka (Matthews et al. 2015), 630 ± 3 ka (Jicha et al. 2016), and 627 ± 3 ka (Mark et al. 2017). U–Pb dating of individual LCT-B zircon faces yield crystallization ages of 626 ± 6 ka (Matthews et al. 2015), and 629 ± 4 ka from whole-grain isotope-dilution thermal ionization mass spectrometry (Wotzlaw et al. 2015). LCT-B zircon are mostly reversely zoned, with zircon faces and some interior zones having brighter cathodoluminescence than their cores with lower U, Th, REE and Hf concentrations, and smaller europium anomalies, which are interpreted as evidence of episodic heating and renewed crystallization in the LCT source reservoir (Matthews et al. 2015). Fe–Ti oxide thermometry suggests apparent eruption temperatures from 820 to 900 °C for LCT-B (Hildreth 1981; Hildreth et al. 1984) and 819 ± 12 °C from Ti-in-zircon thermometry of LCT-B crystal faces (Matthews et al. 2015). Wotzlaw et al. (2015) concluded LCT-B zircons record the rapid assembly of multiple magma reservoirs by repeated injections of isotopically heterogeneous batches of magma with short pre-eruption storage times of 10^3–10^4 years.

Lead isotopes measured in individual LCT sanidine give $^{207}Pb/^{206}Pb$ values of 0.88–0.90 and $^{208}Pb/^{206}Pb$ values of 0.21–0.23, defining a distinct chemical array from post-caldera rhyolites (Watts et al. 2012). Neodymium and strontium isotopes determined in one study for LCT-B bulk are $\varepsilon Nd = -7.8$ and $^{87}Sr/^{86}Sr = 0.71012 \pm 3$ (2σ), which was interpreted as evidence of mafic input into the LCT-B bulk system (Hildreth et al. 1991). Oxygen isotopes measured in LCT-B whole rock along with individual zircon and quartz grains ($\delta^{18}O = +5.3$ to $+6.8$ ‰) suggest a relatively homogenized and equilibrated magma body prior to the caldera-forming eruption with respect to oxygen isotope ratios (Bindeman and Valley, 2001). Glass inclusions in LCT-B

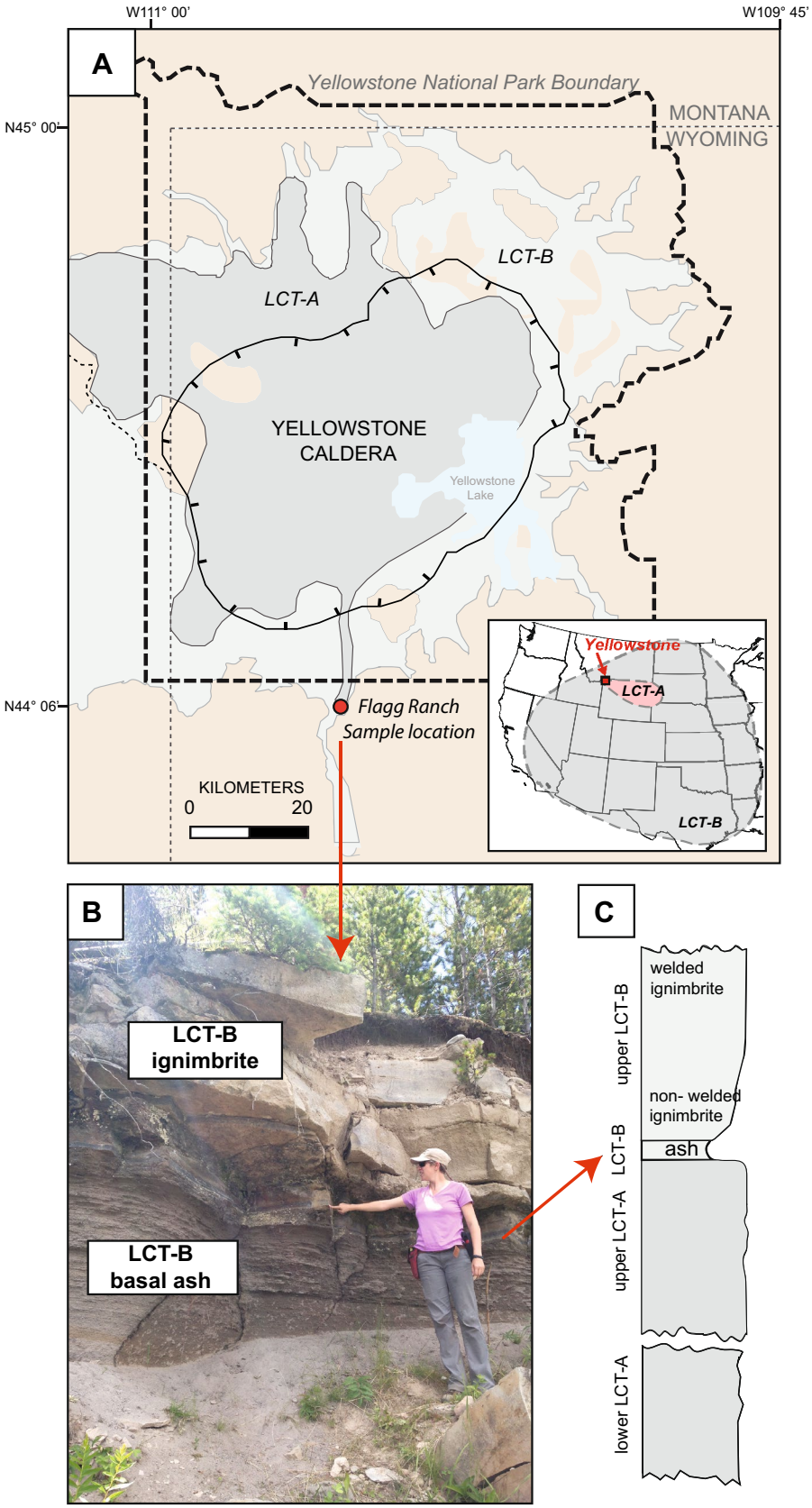

Fig. 1 **a** Geologic map of Yellowstone Caldera (adapted from Matthews et al. 2015). Black solid lines define the caldera outline and ignimbrite sheets of both LCT members A and B are shown in dark and light gray. Red dot denotes sample location at Flagg Ranch, just outside of Yellowstone National Park. Inset of the United States shows ash distribution of the LCT (USGS.gov). **b** Photograph of an outcrop at sample location where the boundary between LCT ash fall and LCT-B ignimbrite are well exposed. **c** Cartoon showing stratigraphic relationship between ignimbrite sheets and fallout ash (adapted from Christiansen 2001; Matthews et al. 2015)

quartz crystals contain H_2O concentrations of 3.2–3.8 wt% (av. 3.4 wt%) and CO_2 concentrations of 200–800 ppm (av. 500 ppm) corresponding to pressures of 100–200 MPa in the presence of volatile-saturated melt (Gansecki 1998). These pressures agree with a variety of geophysical depth estimates for the uppermost portion of the present-day reservoir beneath Yellowstone of ~ 5 km (~ > 100 MPa pressure) (Eaton et al. 1975; Smith and Braile 1994; Smith et al. 2009; Farrell et al. 2014).

Methods and samples

Lava Creek Tuff samples

Bulk ignimbrite and basal fallout ash were collected from just outside Yellowstone National Park at Flagg Ranch, WY, where the contact between LCT-A and LCT-B is well exposed (Fig. 1b). The LCT-B fallout ash deposit (sample 15CTYC-14) is well sorted, containing glassy ash-sized fragments and 17 vol% phenocrysts including sanidine, quartz, and minor amounts of magnetite, ilmenite, fayalite, and zircon. LCT-B ignimbrite overlies the fallout ash and is non-welded with 88 vol% matrix and 12 vol% phenocrysts including feldspar (8%), dominantly sanidine, quartz (3%), and minor (< 1%) magnetite, ilmenite, ferroaugite, fayalite, zircon, chevkinite, and allanite (sample 15CTYC-17). The bulk major and trace element compositions of the ignimbrite and fallout ash were determined by X-ray Fluorescence (XRF) analysis and Inductively Coupled Plasma Mass Spectrometry (ICPMS) at the Washington State University Peter Hooper GeoAnalytical Lab and are given in Online Resource 1.

Sanidine and quartz from the fallout ash were separated for within-grain analyses using wet sieving, magnetic separation, and LST heavy liquids. Euhedral to subhedral sanidine and quartz with few to no inclusions were picked from the resulting mineral separates for further study. Phenocryst sizes vary between 500 and 800 µm in width and 1000–1300 µm in height for sanidine, and ~ 1000 by ~ 1000 µm for quartz. Sanidine (135 grains) and quartz (22 grains) were mounted in epoxy and imaged by cathodoluminescence (CL) on a scanning electron microscope at Stanford University with a 10 kV accelerating voltage and 20 nA current. CL zoning patterns were used to assess which sanidine and quartz to target for future EPMA analysis (e.g., Fig. 2). For phenocrysts with chemical zoning, we define a "rim" as a bright CL zone with distinct crystal habit that spans from the outermost edge of the crystal to a sharp transition to a darker CL interior.

Ion-microprobe major and minor analysis of sanidine and quartz

Compositions of euhedral sanidine and quartz were determined via wave-dispersive spectroscopy using the JXA-8530F Electron Probe Micro-Analyzer (EPMA) at the Eyring Materials Center at Arizona State University. The EPMA was operated at 15 kV and 15 nA using a 5 to 10 µm beam diameter to measure major feldspar-forming elements plus Ba in 20 sanidine grains (Online Resource 2). Analyses of Ti in 4 quartz grains (Online Resource 3) were performed at 15 kV and 200 nA using a 5 to 10 µm beam diameter (operating conditions after Thomas et al. 2010). The reproducibility of standards was typically better than 1 wt% relative for concentrations > 10 wt%, and 10 wt% relative for concentrations of 0.1–1 wt%; thus error is conservatively

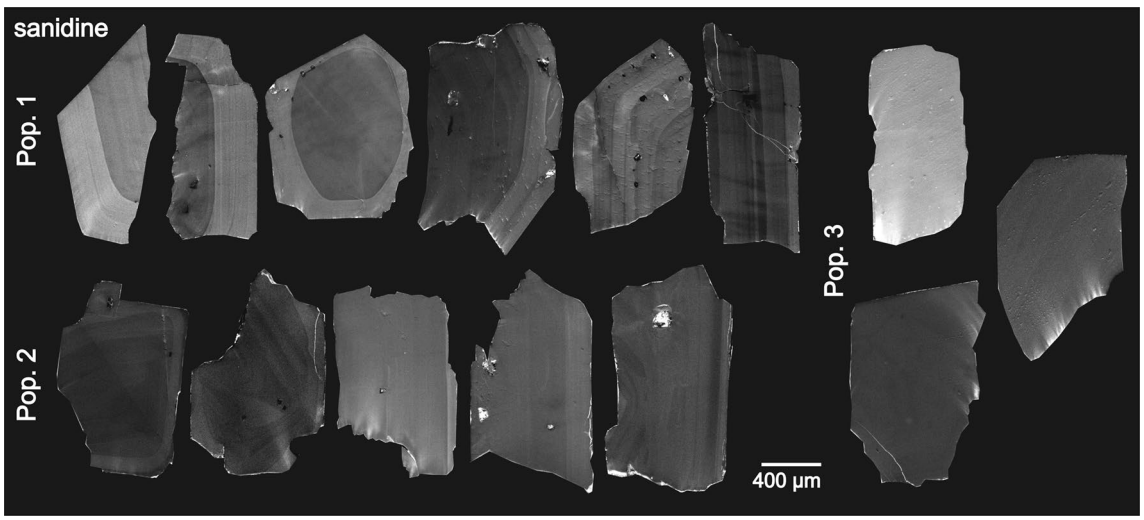

Fig. 2 Cathodoluminescent images of representative LCT-B sanidine from each of the three identified populations

reported as 10 wt% for Ba concentration, 1 mol% for orthoclase content, and < 0.1 wt% for Ti concentration.

NanoSIMS trace element analysis of sanidine

Based on CL and EPMA data, five representative LCT-B sanidine were chosen for trace element analyses with the CAMECA 50L Nano-Scale Secondary Ion Mass Spectrometer (NanoSIMS) in the NSF SIMS-NanoSIMS Facility at Arizona State University. Analyses were made in multi-collection mode using an O^- primary beam with ~ 90–120 pA intensity generating secondary ions with intensities of ~ 100–150 nA. Dwell times were 20 s/pixel. A raster size of 256 × 256 µm was used to measure beam-controlled line scans of ^{24}Mg, ^{30}Si, ^{88}Sr, and ^{138}Ba varying from 40 to 80 µm in length. The ion beam diameter was ~ 0.3 µm with an average of 0.7 µm spacing between each analysis spot. Standardization was performed on NIST glass 610, 612, and 614. Although only the shape of trace element profiles is required for diffusion modeling, absolute concentrations of measured trace elements were calculated by normalizing to Si and referenced to working curves from NIST glasses. 2-sigma error on trace element measurements was calculated as Poisson error using the following equation: $\left[1/\sqrt{\frac{\mathrm{Ba}}{\mathrm{Si}}\mathrm{cts}} \times \mathrm{Ba\ (ppm)}\right]$.

Results

LCT-B geobarometry

Pressure is an important parameter in all the models used in this study; therefore, we determined pressure using two different geobarometers and compared these to previously published estimates. First, we utilized the DEtermining Rhyolite Pressures (DERP) geobarometer, which calculates pressures from the compositions of near-liquidus rhyolitic glass in equilibrium with quartz and at least one feldspar, considering the effect of anorthite and water content (Wilke et al. 2017). Depending on the water content used (1–4 wt% H_2O based on previous LCT work; Gansecki 1998), the DERP-calculated pressures for LCT-B vary between 430–460 MPa for the bulk ash (sample 15CTYC-14) or 230–260 MPa for the glass composition (7YC-325, Gansecki 1998). Second, we utilized the rhyolite-MELTS geobarometer (MELTS_Excel; Gualda et al. 2012; Gualda and Ghiorso 2014), which yields a pressure range of 80–150 MPa for 1–4 wt% H_2O for the LCT-B bulk composition. Rhyolite–MELTS estimates are consistent with storage pressures determined from recent melt inclusion data for LCT-B (up to 150 MPa; Befus et al. 2018) and the estimated depth of the present crustal magma reservoir as determined by seismic tomography (Farrell et al. 2014). The discrepancy in the estimated pressures may be rooted in the calibrated range of An-contents of the DERP model (3.5–7.0 mol% An; Wilke et al. 2017), whereas LCT-B feldspar has much lower An-content (1.3–2.7 mol% An). Additionally, due to the nature of the model calibration, the DERP geothermometer consistently predicts higher pressures than rhyolite-MELTS (Ghiorso, personal comm., May 2018). Therefore, for the purpose of this paper, we favor the pressures returned by rhyolite-MELTS and use these values for further modeling.

Sanidine compositions and thermometry

Sanidine from LCT-B fallout ash were grouped into three populations based on CL-zoning patterns, orthoclase content, Ba concentrations and their relative estimated temperatures. As shown in Fig. 2, Population 1 grains are euhedral to subhedral, blocky to tabular, and reversely zoned with bright CL rims (20–300 µm thick) that terminate core-ward at a sharp "step-zoned" contact. Overall, Population 1 has Ba concentrations ranging from 1000 to 7000 ppm with relatively low orthoclase content ($Or_{44–54}$) (Fig. 3). These sanidine exhibit variable zoning patterns including single thick (130–300 µm) bright CL rims overgrown on a dark CL core, or relatively thin (30–120 µm) bright CL rims that mantle

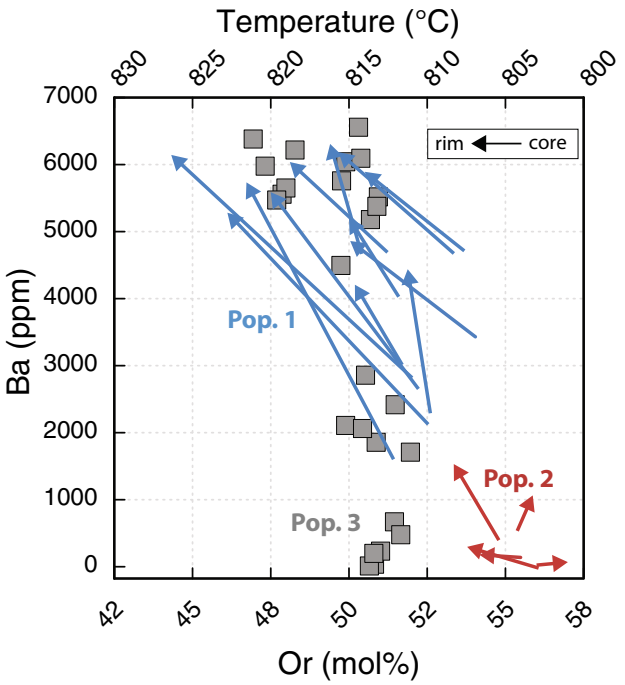

Fig. 3 EPMA data of LCT-B sanidine populations. Population 1 and 2 arrows depict the change in chemistry across core-to-rim boundary in zoned sanidine. Population 3 data points (grey boxes) are spot analyses across unzoned sanidine grains. Temperature shown here was calculated using Putirka (2008) feldspar-liquid thermometer with a standard error of ± 23 °C

oscillatory zoned interiors (Fig. 2). Crystal rim-core boundaries reveal resorption and regrowth textures where rims sometimes truncate preexisting zones with various degrees of grain boundary rounding. Population 1 is best suited for further analysis because of their well-defined euhedral edges suggesting they record conditions immediately before eruption. They also represent > 50% of the total sanidine grains inspected and therefore thought to be volumetrically dominant in LCT-B and thus were investigated in greatest detail for the purpose of this study.

Population 2 represents ~ 30% of LCT-B sanidine and is characterized by subhedral, tabular grains with relatively thin (30–60 µm) bright CL rims. Some grains have uniform CL interiors and others have progressive oscillatory zoned interiors (Fig. 2). These sanidine have a narrower range in their chemical properties compared to Population 1, including lower Ba concentrations ranging from below the detection limit (~ 4 ppm) to 2500 ppm as well as have higher orthoclase content ($Or_{53–57}$) (Fig. 3). Population 2 crystals also show resorption and regrowth textures described for Population 1.

Population 3 sanidines are anhedral, mostly fragmented, have an orthoclase content similar to Population 1 ($Or_{47–52}$), and have the widest range in Ba concentrations of the three populations, ranging from below the detection limit (~ 4 ppm) to 6500 ppm. These sanidine lack both distinct CL patterns and well-defined crystal rims (Fig. 2) and thus were not investigated further in this study.

The Putirka (2008) alkali-feldspar-liquid thermometer (reported standard error of ± 23 °C) was applied to the sanidine compositions collected in this study from LCT-B fallout ash in combination with the glass composition from LCT-B ignimbrite pumice (samples 8YC-411 and 7YC-325 reported by Christiansen 2001). The calculations assume pressures between 80–150 MPa, which represent the calculated pressures from the rhyolite-MELTS geobarometer discussed above. On average, core to rim changes in orthoclase content are 2–8 mol% for Population 1, and 2–3 mol% for Population 2 sanidine. Feldspar-liquid thermometry suggests an average rim temperature of 814 ± 23 °C at 100 MPa with a temperature increase at the core-rim boundary of ~ 10 °C for Population 1 and ~ 5 °C for Population 2. Although these changes in temperature are within error of the thermometer (SEE ± 23 °C; Fig. 4), we interpret these variations as real changes in temperature as they are correlated to variations in orthoclase content determined with very small error (± 1 mol% orthoclase). Furthermore, when the analytical error on major element oxide measurements via EPMA analysis was propagated to determine the range in absolute temperature values, we find very small error of ± 1 °C. Therefore, although the reported thermometry results for LCT-B sanidine zones may vary by ± 23 °C, the relative changes in temperature from crystal core to rim appear to be robust.

In conjunction with feldspar-liquid thermometry, we utilize alkali-feldspar composition–temperature relationships, predicted by rhyolite-MELTS (version 1.1.0), as a secondary thermometer. To this aim, we modeled LCT-B bulk composition to determine alkali–feldspar–liquid equilibria as function of temperature at the appropriate pressures (100–300 MPa) over a range of water contents (1–4 wt% H_2O). We then use a linear fit to obtain an equation that predicts temperature from feldspar orthoclase-albite ratio facilitating the determination of temperatures relevant to our natural LCT-B sanidine compositions where the coexisting melt composition is unknown, for example, for their core compositions (Fig. 5). Rhyolite-MELTS (Gualda et al. 2012; Ghiorso and Gualda 2015) has been shown to effectively reproduce the crystallization sequence and compositions of felsic phases in rhyolitic systems (e.g., the Bishop Tuff), particularly the crystallization relationship of sanidine and quartz (Gardner et al. 2014). Although Gardner et al. (2014) found the absolute temperatures predicted by rhyolite-MELTS overestimates absolute crystallization temperatures constrained by experiments by ~ 40 °C, in general, rhyolite-MELTS and the Putirka (2008) feldspar–liquid thermometer predicted temperatures within error of each other (e.g., Fig. 4). Rhyolite-MELTS modeling predicts a temperature increase at the core-rim boundary (associated with changes in feldspar composition) of ≥ 10 °C for both Population 1 and 2 assuming conditions of 3 wt% H_2O and 100 MPa. When the orthoclase-albite–temperature relationships for lower water contents are used (1–2 wt% H_2O), the core-rim boundaries yield slightly greater temperature changes, up to 20 °C (Fig. 5). Generally, this temperature range would change if crystallization accompanied decompression, which is discussed in later sections. Similar to feldspar–liquid thermometry temperature estimates, we propagated the analytical uncertainty on major element XRF analyses of the bulk composition of LCT-B, which yielded ± 35 °C in the absolute temperature estimates by rhyolite-MELTS. Similar to discussion above on feldspar–liquid thermometry, although there may be error in the absolute temperatures, we find the magnitude of the core-rim temperature variations predicted by rhyolite-MELTS to be robust.

Quartz composition and thermometry

LCT-B quartz from fallout ash are euhedral to subhedral grains with reverse zoning in CL. Some grains have relatively thick (100–200 µm) bright CL rims, well-defined crystal edges, and sharp boundaries between rims and dark CL cores (Fig. 6a) similar to the Population 1 sanidine (Fig. 2), while others are characterized by oscillatory zoning with thin (25–90 µm) bright CL rims and diffuse intra-crystalline boundaries. Overall, LCT-B quartz exhibit resorption and regrowth textures with rims truncating interior zones with

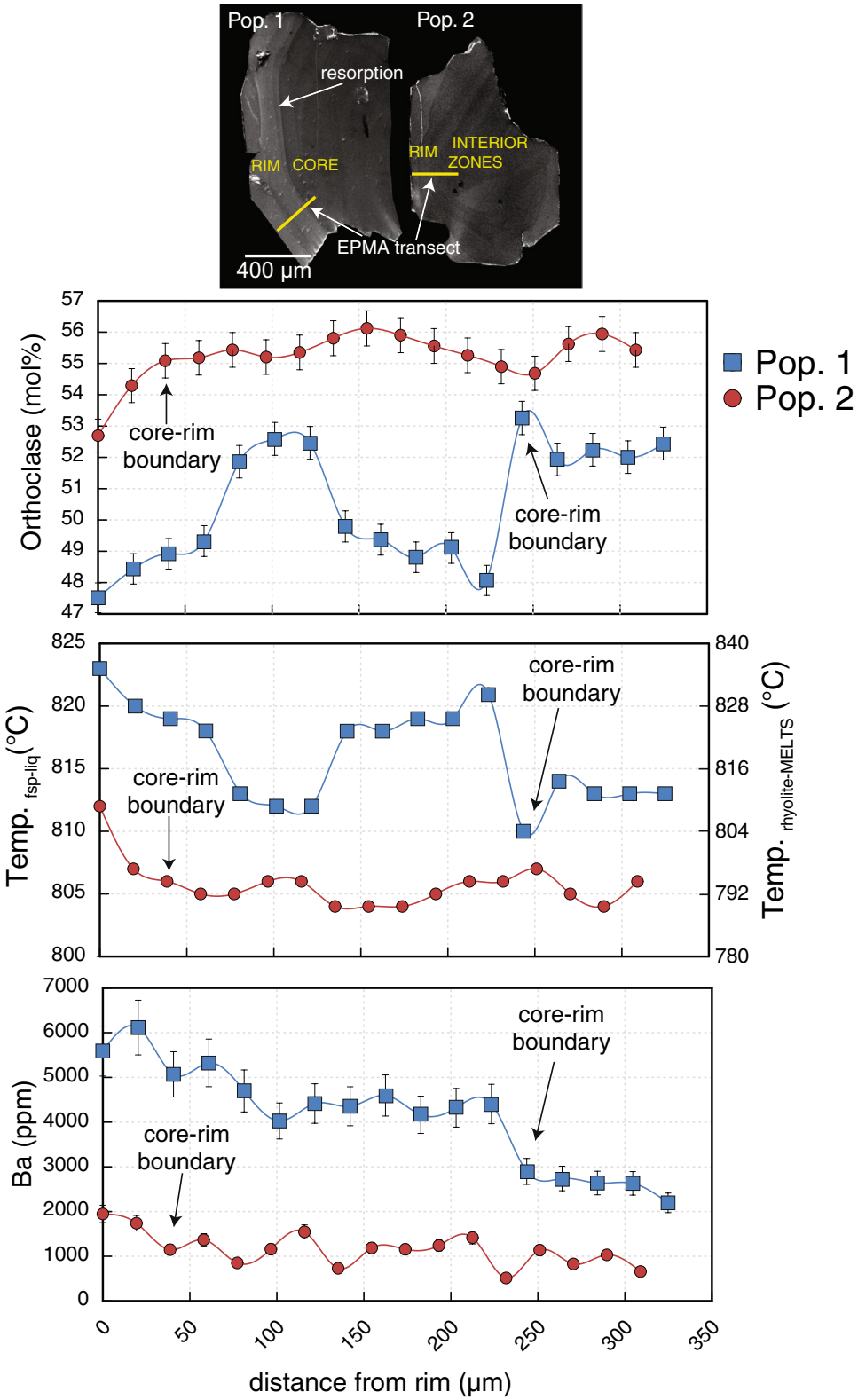

Fig. 4 EPMA transects of two representative sanidine from Population 1 and 2. Bright CL rims are associated with increases in Ba concentration, decrease in orthoclase content, and slight increase in temperature in both feldspar-liquid thermometry and rhyolite-MELTS thermometry assuming conditions of 3 wt% H_2O and 100 MPa. Temperature estimates from feldspar-liquid thermometry and rhyolite-MELTS show absolute temperature estimates within error [SEE ± 23 °C (Putirka 2008), ± 35 °C rhyolite-MELTS] but still reflect real temperature fluctuations based on orthoclase variation (see text for further discussion). Population 1 sanidine have greater variation in these properties from core to rim compared to Population 2 grains. The error on Ba is smaller than symbol size in some instances

various degrees of rounding, similar to Populations 1 and 2 sanidine. EPMA analysis shows an average increase in Ti concentration from core to rim of 20 ppm, with average rim concentrations of 40–80 ppm Ti.

Titanium-in-quartz thermometry (TitaniQ; Wark and Watson 2006) for LCT-B quartz rims was conducted over a pressure range of 80–150 MPa consistent with the geobarometry discussed above, at a constant a_{TiO_2} of ~0.33 as

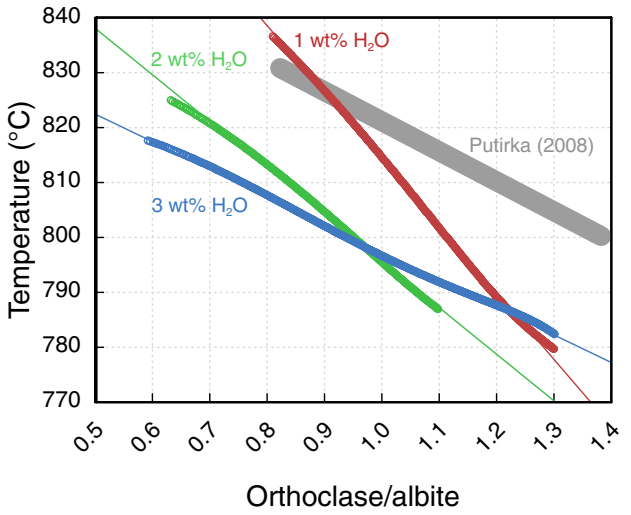

Fig. 5 Rhyolite-MELTS predicted relationships between temperature and orthoclase–albite ratio assuming 100 MPa and variable water contents. Each trend is linearly fit and used as a thermometer to predict temperatures for LCT-B sanidine orthoclase–albite ratios. Grey thick line represents LCT-B (Population 1 and 2) sanidine core and rim compositions with temperatures predicted by feldspar-liquid thermometry (standard error of ±23 °C not shown; Putirka 2008)

suggested by other Yellowstone lavas similar in major element chemistry as LCT-B (e.g., Solfatara flow, Vazquez et al. 2009). Here we use the Huang and Audétat (2012) TitaniQ calibration, wherein the activity term is included in the equation, as indicated by Hayden and Watson (2007), and returns a relative temperature increase across rim-core boundaries of 30–50 °C. Although TitaniQ requires important assumptions to determine absolute temperature, the relative temperature change from core to rim remains the same regardless of the chosen activity and pressure. The average temperature for quartz rims varies from 760–850 °C ± 35 °C (av. 815 °C) corresponding to the range of activities and propagated analytical error via EPMA. Although a_{TiO_2} is assumed constant for these calculations, which may not be the case in nature, a temperature increase from quartz core to rim is still resolvable. For example, in the hypothetical scenario where a rejuvenation event is accompanied by remelting of the resident LCT-B reservoir, where a_{TiO_2} increases (e.g., $a_{TiO_2}=0.33$ to $a_{TiO_2}=0.6$, the total range of Yellowstone lavas reported by Vazquez et al. (2009)), would correspond to an absolute temperature change of only 8 °C in TitaniQ. Thus, even in this scenario, changes in quartz composition correspond to temperature increases > 20 °C.

Modeling LCT-B bulk system to constrain pre-eruptive conditions

The sequence of crystallization for LCT-B bulk ash composition was determined using rhyolite-MELTS (Gualda et al. 2012; Ghiorso and Gualda 2015). For these compositions, the ferrous–ferric ratios were determined via MagmaSat and isobaric crystallization was modeled between 1250 and 500 °C. Isenthalpic mode (−50 J) allowed for better determination of the ternary minimum and greater resolution in temperature as this mode allows the temperature to vary at each step along the calculation path (Gualda et al. 2012; Ghiorso and Gualda 2015). The models were run with a range of initial water contents (1–4 wt% H_2O) and a CO_2 concentration of 500 ppm suggested by melt inclusion data for LCT-B ash (Gansecki 1998). Modeling at 100 MPa and

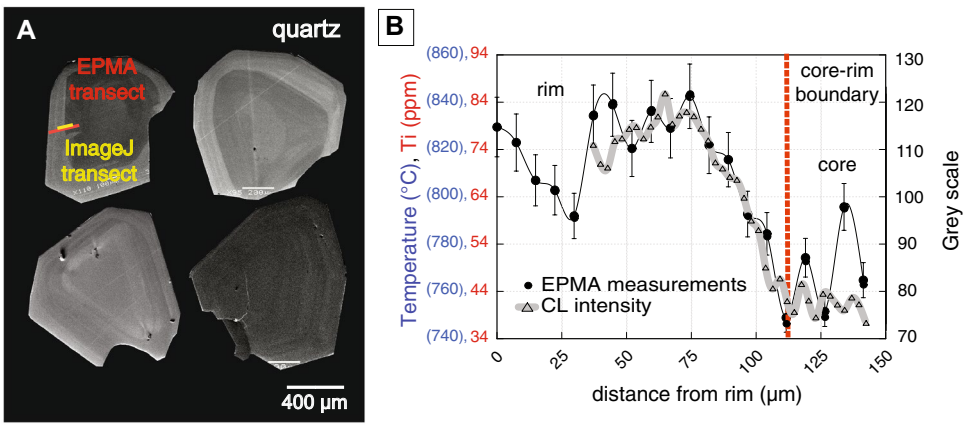

Fig. 6 **a** Cathodoluminescent images of LCT-B quartz grains with variable zoning patterns. Location of a longer EPMA transect (red) and shorter ImageJ transect (yellow) are included. **b** Ti concentration profile analyzed via EPMA (black circles) overlaid by CL intensity profile (grey triangles) extracted from a CL image using ImageJ software, illustrating the correlation between Ti concentration and CL intensity similar to what is observed by Leeman et al. (2008). TitaniQ temperatures are also shown (values in parenthesis) with a relative temperature increase towards the outermost rim. Error bars represent ±5 ppm Ti per the reproducibility of standards on EPMA. Error from Ti measurements and variation in activity were used to assess error on temperature calculations of ±35 °C (not shown, see text for discussion)

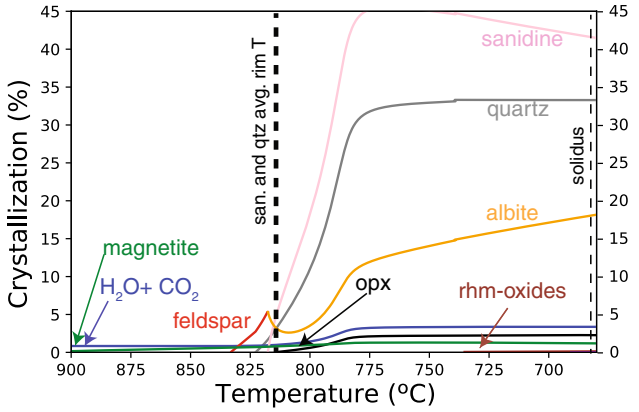

Fig. 7 Phase diagram of the bulk LCT-B system predicted by rhyolite-MELTS modeling at 3 wt% H_2O under isenthalpic and isobaric conditions of 100 MPa. Sanidine and quartz rim temperatures calculated via thermometry are shown by dashed line

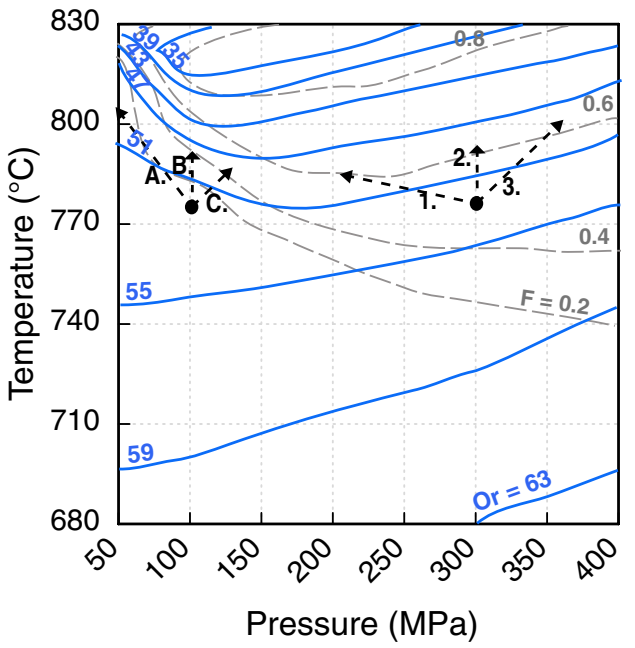

Fig. 8 Phase diagram showing the stability of variable orthoclase using rhyolite-MELTS predicted pressure-temperature-composition data for the LCT-B bulk composition at 3 wt% H_2O. Blue contour lines represent orthoclase content, and grey dashed lines are melt fraction contours. Two sets of black arrows are shown as trajectories showing three major possibilities to achieve the orthoclase change from core to rim observed in LCT-B sanidine (av. Or_{52} to Or_{49}) if assuming a starting pressure of 100 MPa (A–B) or 300 MPa (1–3), for example. Note we favor the set of trajectories at 100 MPa, as it corresponds to geobarometry estimates

3 wt% H_2O, as suggested by both geobarometry and melt inclusion estimates discussed above, produces a crystallization sequence with magnetite as the liquidus-phase at 920 °C, followed by feldspar at 830 °C, quartz at 820 °C, and the feldspar solvus at 820 °C, below which sanidine and albite crystallize under fluid-saturated conditions (Fig. 7). Although the crystallization conditions of mafic phases are less reliable in rhyolite-MELTS (Gardner et al. 2014), the model predicts orthopyroxene and rhombohedral-oxide crystallization at 810 °C and 740 °C, respectively. At 814 °C, the average temperature of LCT-B sanidine and quartz rims, the modeled bulk system consists of 85% melt, 6% sanidine, 4% quartz, 3% albite, 0.8% magnetite, 0.2% orthopyroxene, and 1% fluid (48 wt% CO_2: 52 wt% H_2O) (Figs. 7, 8). This crystal assemblage closely reflects the modal abundance of the natural ash sample (sample 15CTYC-17). Over the temperature interval relevant to both LCT-B sanidine and quartz predicted by thermometry, rhyolite-MELTS supports that sanidine and quartz are co-saturated, a phenomenon commonly observed in the haplogranite ternary system (e.g., Gualda and Ghiorso 2014; Bachmann and Huber 2016). Therefore, we invoke that LCT-B sanidine and quartz represent two major phases indicating crystallization in a system that was simultaneously reheated.

In addition to modeling the sequence of crystallization, a series of successive isobaric crystallization models (runs over a conservative pressure range of 50–400 MPa) were compiled to construct a phase diagram (Fig. 8). Feldspar orthoclase content (solid blue lines) and bulk melt fraction (dashed gray lines) are used to determine pressure–temperature (*P–T*) trajectories that could reproduce the observed major element zoning in LCT-B sanidine. The results from rhyolite-MELTS and the derivative phase diagram suggest, in all cases, an increase of ~ 10 °C is necessary to produce the average change from Or_{52} cores to Or_{49} rims observed in the LCT-B Population 1 sanidine. Two sets of trajectories are shown assuming starting pressures of 100 MPa and 300 MPa. Note that we favor 100 MPa per the geobarometry results explained in previous section. The *P–T* trajectories that reproduce the observed change in sanidine composition from core to rim include: (1) decompression of 50–100 MPa during heating, (2) an isobaric heating event or, and (3) an increase in pressure of ~ 25–50 MPa during heating.

Timescales via diffusion modeling

Diffusion chronometry utilizing NanoSIMS Ba and Sr concentration profiles in sanidine was conducted on five representative crystals from Population 1 (Online Resource 4). Changes in Ba concentration from core to rim were on the order of 2000–4000 ppm for Population 1 grains and 1000 ppm for those in Population 2 (Fig. 4). Diffusion chronometry was also conducted on LCT-B quartz grains; however, analysis of Ti concentration in quartz is challenging due to its relatively low abundance and limited spatial-resolution on the EPMA. Like many other studies (e.g., Wark and Watson 2006; Wark et al. 2007; Matthews et al. 2012;

Leeman et al. 2012; Gualda et al. 2012; Gualda and Sutton 2016), we observed a correlation between Ti concentration and CL intensity (Fig. 6b), and thus utilized CL intensity as a quantitative proxy for Ti concentration in quartz. CL intensity profiles were extracted using ImageJ (Schneider et al. 2012) image processing software on six LCT-B quartz grains (Online Resource 5).

Modeling assumed a step-function initial condition and employed an analytical solution to Fick's Second Law, involving one-dimensional diffusion in an infinite medium with an abrupt change in composition when the diffusion distance is small (Costa et al. 2011):

$$C = C_0 + \frac{C_1 - C_0}{2}\left[erfc\frac{x}{2\sqrt{Dt}}\right], \quad (1)$$

where C is the normalized concentration, C_0 and C_1 are the initial amounts of the elements on each side of the interface at time zero, D is the diffusivity ($m^2\ s^{-1}$), t is the diffusion time, and x is the midpoint on the concentration profile. Diffusivities were calculated using Eq. (2) using the Arrhenius parameters determined by Cherniak (1996, 2002), and Cherniak et al. (2007) specified in Table 1. For sanidine, modeling assumed a constant temperature of 814 °C representing the average rim temperature as determined by feldspar–liquid and rhyolite-MELTS thermometry. For quartz, the modeling was conducted at a range of temperatures between 760–850 °C, representing quartz rim temperatures determined by TitaniQ specified above.

$$D = D_0 e^{\left(\frac{-E}{RT}\right)}. \quad (2)$$

We used a least-square minimization procedure to find the complementary error function that best fit each observed trace element profile by varying the concentration of each plateau, the center of the diffusion profile, and the diffusion length scale ($\sqrt{Dt}$).

When modeled at a constant temperature of 814 °C, the Ba in sanidine profiles suggest average timescales on the order of 1 ky, while the Sr in sanidine profiles suggest average timescales on the order of ~ 0.02 ky (Fig. 9, Online Resource 4). If produced by the same event, the Ba and Sr profiles should yield similar timescales despite their different diffusivities. Additionally, because Sr diffuses faster than Ba, the width of the Sr profile should be greater than that of Ba for a given time interval (Table 1). However, in almost all cases the Ba and Sr profiles are of equivalent width and in one case, the Sr profile is shorter than the Ba profile (Online Resource 4), which is the opposite of what is expected. This suggests that the profiles did not originate as step-function concentration profiles subsequently altered by only diffusive relaxation. Till et al. (2015) observed similar behavior in Ba and Sr concentration profiles across sanidine core-rim boundaries from a post-caldera rhyolite at Yellowstone and concluded the profile originated during rim growth in an evolving melt composition with little to no subsequent diffusion. Here we draw the same conclusion, which is also supported by the relative rates of diffusion versus crystal growth in sanidine [i.e., sanidine growth rates (10^{-8}–10^{-12} m s^{-1};

Table 1 Arrhenius parameters and calculated diffusivities

	D_0 (m^2/s)	E (kJ/mol)	Diffusivity at 814 °C (m^2/s)	Profile width at 814 °C for 5 years (μm)
Sanidine				
Ba[a]	0.29	455	3.9E−23	0.5
Sr[b]	8.4	450	2.0E−21	3.5
Quartz				
Ti[c]	7.0E−08	273	5.3E−21	6.0

[a]Cherniak (2002), [b]Cherniak (1996), [c]Cherniak et al. (2007)

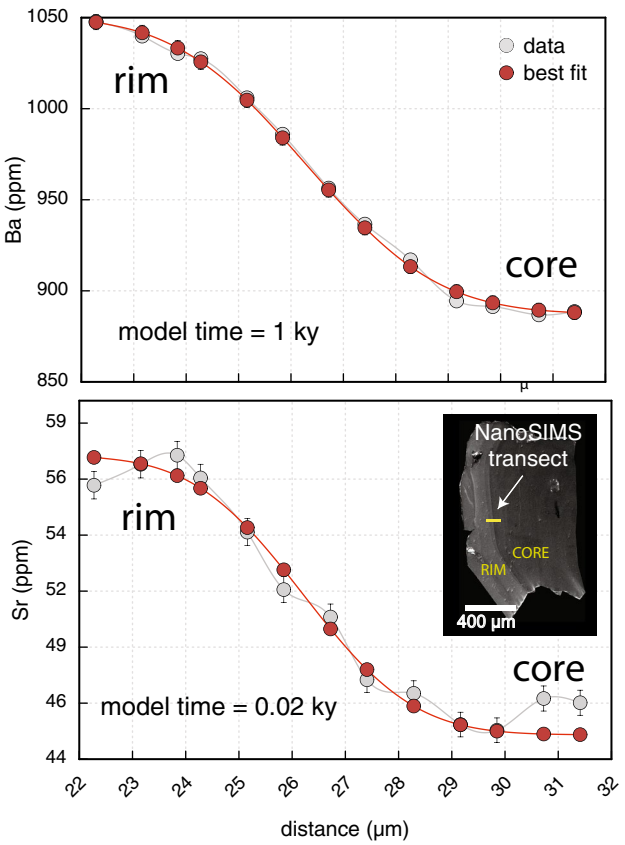

Fig. 9 NanoSIMS trace element profiles across core-rim boundary for a representative Population 1 sanidine. The best fit model calculated via diffusion chronometry is shown in red at an assumed temperature of 814 °C with a step-function as an initial condition. NanoSIMS transect (yellow) direction is from rim (left) to core (right) as shown on CL image provided. Error bars are smaller than symbol size in the case of Ba measurements

Swanson 1974, 1977) are far faster than Ba and Sr diffusion (10^{-22}–10^{-23} m^2 s^{-1}; Table 1)]. In this situation, any timescale calculated via diffusion modeling of Ba or Sr relaxation from a step function will represent a significant overestimation of the time it took for the rim to form. Instead, diffusion chronometry requires the comparison of the Ba and Sr concentration profiles with that of a very slow diffusing element at magmatic conditions, such as CaAl–NaSi exchange in plagioclase that can be used as a proxy for an initial profile shape prior to diffusion. However, at present, we lack such data on similarly slow diffusing elements for sanidine. Because the Ba and Sr concentration profiles are identical in shape and width in four of five grains modeled, we instead constrain a maximum possible time interval between sanidine rim growth and eruption by determining the time required for the faster diffusing Sr to diverge in shape from the Ba profile using a finite difference approach similar to Till et al. (2015). This approach yields maximum timescales of 10–20 years between rim growth and eruption for the LCT-B sanidine at 814 °C. Therefore, we infer the Population 1 high-Ba and -Sr sanidine rims formed less than 10–20 years prior to the eruption.

For quartz diffusion modeling, a step-function initial condition was assumed in the absence of comparison to other trace elements with varying diffusivities. We utilize 790–815 °C for the average quartz rim growth temperature during modeling as it corresponds to the preferred pressure range of 80–150 MPa from geobarometry and is within error of the sanidine rim thermometry. Modeling at average rim temperature 815 °C yields timescales of 3–40 years, and in one case 300 years (Fig. 10, Online Resource 5). Without the concentration profiles for elements with differing, well-constrained diffusivities, we take these timescales to represent maxima.

Timescales via crystal growth rates

In the absence of a faster diffusing element in sanidine and a second element with different diffusivity in quartz, we also examined crystal growth rate estimates for feldspar and quartz in rhyolitic melts to compare to the maximum timescales determined through diffusion chronometry. Crystal growth rates from both experimental observations and natural samples for felsic magmas, under pressure and temperature conditions relevant to this study, suggest a range between 10^{-8} and 10^{-12} m s^{-1} for both feldspar (Swanson 1974, 1977; Fenn 1977; Zellmer and Clavero 2006; Calzolaio et al. 2010), and quartz (Swanson 1974, 1977; Gualda and Sutton 2016). Assuming the slowest growth rate for both feldspar and quartz (10^{-12} m s^{-1}) produces conservative estimates of 7 months to 20 years (av. 5 years) for the growth of LCT-B feldspar rims, and 7 months to 4 years (av. 2 years) for LCT-B quartz rims. These calculated growth timescales assume a constant growth rate or linear behavior, where temperature and pressure are kept constant, and growth is therefore proportional to time (Zhang 2008). In nature, however, this is likely not the case. Therefore, given the uncertainty in experimentally derived crystal growth rates applied to natural systems, we favor the timescales predicted by diffusion chronometry for sanidine and quartz. Thus, the data suggest that the LCT sanidine and quartz rims grew less than a couple of decades prior to eruption.

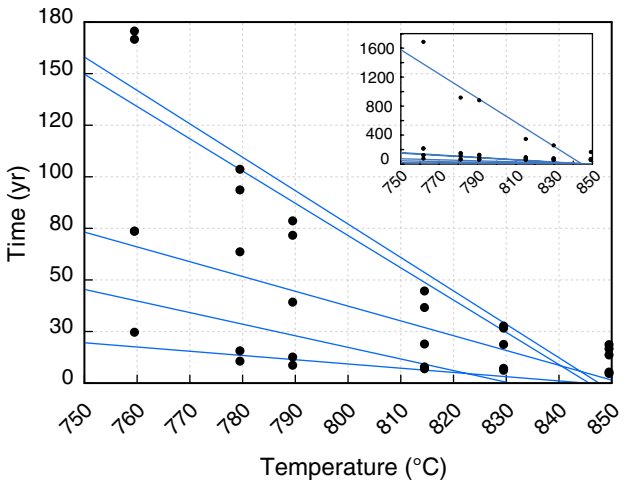

Fig. 10 The range of possible timescales at a given crystallization temperature for LCT-B quartz rims modeled over a range of pressures (100–300 MPa) assuming a constant a_{TiO_2} of 0.33 (Vazquez et al., 2009). Symbols represent the rim temperatures determined for one quartz grain. Lines are linear fits for the range of timescales and temperatures for a single grain to illustrate the relationship between time and temperature-dependent diffusion. Inset shows an outlier grain with relatively long timescales not shown in the range of the main plot

Discussion

LCT-B magmatic history reconstructed through the phenocryst record

The chemical zoning patterns and diffusion chronometry of volcanic phenocrysts are increasingly used as a record of the changes in magma's history preceding eruption, but rarely is a distinct triggering mechanism responsible for an eruption thoroughly resolved. Before assessing plausible eruption triggers, however, we must first constrain the processes recorded in the LCT-B phenocrysts. LCT-B sanidine and quartz both possess resorption textures at their core-rim boundaries and reverse-zoning with bright CL rims with elevated Ba and Sr concentrations in the case of sanidine, and elevated Ti in the case of quartz. Both phases also record a ubiquitous increase in rim crystallization temperatures

compared to their interiors. Together these phenocrysts suggest a composite history including the following sequence of events; (1) the growth of phenocryst cores (which are sometimes oscillatory, suggesting complex early histories), (2) subsequent heating and crystal resorption, followed by (3) growth of sanidine and quartz rims with elevated magmaphile element concentrations (Ba, Sr, Ti) in decades or less prior to eruption, as suggested by diffusion chronometry and growth rates (Figs. 3, 4, 6, 8, 9). In the following section we interrogate a series of possible magmatic processes responsible for the LCT-B phenocryst record, a number of which are motivated by the *P–T* paths necessary to produce the LCT-B sanidine shown in Fig. 8. These possibilities include (a) fractional crystallization, (b) decompression, (c) the addition of volatiles into the magmatic system, and/or (d) a replenishment of less-evolved material into the system (e.g., rejuvenation or underplating event), as well as related thermal and decompression-induced changes in elemental partitioning.

Fractional crystallization and trace element partitioning

The bulk partition coefficients for Ba and Sr for LCT-B whole rock composition are controlled by their relative compatibility in feldspar and quartz, the two most abundant phases (60%, 30%) of the LCT phenocryst assemblage. Thus, progressive fractionation of sanidine from the host magma would decrease Ba and Sr concentrations in the sanidine from core to rim (the opposite of which is observed). Furthermore, Ba and Sr feldspar–liquid partitioning is not temperature- or pressure-dependent. Rather, the partitioning of Ba and Sr in alkali-feldspar has been shown to be heavily dependent on major element feldspar chemistry or orthoclase content for silicic melt compositions (Long 1978; Smith and Brown 1988; Guo and Green 1989; Blundy and Wood 1991; Icenhower and London 1996; Ren 2004). Therefore, the decrease in orthoclase content within LCT-B rims (Fig. 3), should be accompanied by a decrease in Ba and Sr content. Again, this is the opposite of what is observed, suggesting fractional crystallization and changes in partitioning are not responsible for the formation of the chemical profiles observed in LCT-B sanidine rims.

Similarly, LCT-B quartz rims are enriched in Ti. This is a common observation for quartz phenocrysts in silicic magmas and Ti-rich rims overgrown on Ti-poor cores have been interpreted to reflect either (1) a temperature increase (e.g., Müller et al. 2003; Wark et al. 2007), (2) a pressure decrease (Wark and Watson 2006; Cherniak et al. 2007; Thomas et al. 2010; Huang and Audétat 2012; Gualda and Sutton 2016), (3) the addition of CO_2 into the magma (Gansecki 1998; Wark et al. 2007; Blundy et al. 2010) and/or (4) the build-up of a boundary layer in the melt followed by rapid growth (Pamukcu et al. 2016). A temperature increase is observed in LCT-B quartz rims and could explain the elevated Ti concentrations in the quartz rims. The other scenarios are explored further below.

Decompression

Decompression is often accompanied by an increase in temperature (e.g., Figure 8, scenario A/1) due to the latent heat of crystallization (e.g., Blundy et al. 2006). For example, for the case of a slowly ascending H_2O-saturated rhyolite melt, thermodynamic calculations suggest temperature increases on the order of 25 °C for a 200 MPa pressure drop, or 2.3 °C per 1% of plagioclase crystallization (Couch et al. 2003; Blundy et al. 2006). The maximum change in pressure consistent with the observed decrease in orthoclase content in LCT-B sanidine rims (150 → 50 MPa: Fig. 8, scenario 1/A), would thus produce an increase in temperature of ~ 10–20 °C. This pressure drop is also consistent with the temperature change suggested by both rhyolite-MELTS and feldspar-liquid thermometry. The same logic follows for LCT-B quartz. TitaniQ thermometry suggests a temperature increase from crystal core to rim of 30–50 °C (± 35 °C), and like LCT-B sanidine, latent heat of crystallization can account for ~ 10–20 °C or potentially more. Given its explosive nature, it is likely that the ascent rate for the LCT-B ash was much quicker than what was invoked in Couch et al. (2003) and Blundy et al. (2006), such that it could account for > 20 °C of heating in some situations.

Decompression would also result in an increase in Ti-in-quartz partitioning, which is difficult to distinguish from an increase in magmatic temperatures (Wark and Watson 2006; Thomas et al. 2010; Huang and Audétat 2012), similar to what was recently invoked to explain high-Ti quartz rims formed within a year of eruption invoked for the Bishop Tuff (Gualda and Sutton 2016). Thus, decompression-driven crystallization (combined with pressure-dependent changes partitioning for the quartz) explains the chemical and thermal profiles recorded by LCT-B sanidine and quartz, although it does not fully explain the resorption textures observed between the phenocryst cores and rims.

Addition of CO_2

Another mechanism possible to facilitate crystal growth and the Ti-enrichment in quartz includes the interaction of CO_2-rich vapors from a deeper and less-evolved body with shallowly stored magma (e.g., Blundy et al. 2010; Oppenheimer et al. 2011; Iacovino 2015; Humphreys et al. 2016). There is some evidence to suggest CO_2 is an important player in the LCT source region, where the injection of a less-evolved magma either accompanied or followed isobaric fluid-saturated crystallization (e.g., Fig. 8, scenario B/2), a mechanism invoked to explain the variability of

CO_2 (100–760 ppm) compared to H_2O (3.2–3.8 wt%) in quartz-hosted melt inclusions in LCT-B fallout ash (Gansecki 1998). The rhyolite-MELTS modeling in this study that best matches the LCT-B phenocryst rim thermometry also suggests that LCT-B sanidine and quartz rims were crystallizing in the presence of a fluid rich in CO_2 (Fig. 7). While the addition of CO_2 could act as the driving force for crystallization of LCT-B phenocryst rims and supply the temperature increase through the latent heat of crystallization, this mechanism alone cannot explain the trace element distribution in sanidine and quartz (e.g., Figs. 4, 6) based on the associated partitioning behavior previously discussed.

Rejuvenation and/or underplating

Even in the most favorable scenario discussed thus far, decompression alone fails to explain the resorption textures observed between the cores and rims in LCT-B sanidine and quartz. Underplating of more juvenile material would supply heat and potentially melting to the LCT-B reservoir, such that resorption textures could develop on the phenocryst cores, and enrich the melt in magmaphile elements (Ba, Sr, Ti). However, at the relevant temperatures, Ba and Sr would diffuse 200 and 900 μm in 20 years, exceeding the average Population 1 rim thickness (160 μm), precluding the likely buildup of an enriched melt-layer around feldspar as Pamukcu et al. (2016) suggested. Melting crystals via underplating could still enrich the ambient melt in Ba, Sr, and Ti; however, it is difficult to know by how much. Thus, we cannot rule out underplating, although it is not our preferred mechanism for providing the trace element enrichment in the phenocryst rims.

The simplest explanation for both the resorption of the feldspar and quartz cores and the subsequent chemical and thermal profiles recorded in their rims is a replenishment of more juvenile magma into the preexisting mush (e.g., Ginibre et al. 2004; Stelten et al. 2013; Bachmann et al. 2014; Till et al. 2015). Of the possible mechanisms that can produce the observed core to rim orthoclase variation in LCT-B sanidine, we favor scenario A/1 where LCT-B bulk system first experiences the addition of rejuvenation material leading to heating and resorption textures as well as enrichment in magmaphile elements, followed by decompression to catalyze the rim crystallization with the observed thermal and chemical characteristics.

Invoking rejuvenation to explain LCT-B phenocrysts is consistent with related Yellowstone studies that find the injection of juvenile magma is an important mechanism in the formation of Yellowstone lavas erupted after LCT (Stelten et al. 2013, 2015, 2017; Till et al. 2015). In addition, LCT-B zircons exhibit crystal faces with less-evolved compositions and are interpreted to record episodic heating and/or new magma input (Matthews et al. 2015). The change in chemistry recorded by LCT-B phenocryst rims is not significant enough to require the addition of a mafic magma, rather; it is more likely that a magma body with similar major element chemistry (i.e., rhyolitic) but with higher concentrations of compatible trace elements (relative to LCT-B cores), which is the same scenario interpreted for post-LCT rhyolite lavas based on their Hf and O isotope compositions in zircon (Stelten et al. 2013, 2015, 2017).

Implications of phenocryst populations

Recall, there are three populations of LCT-B sanidine, as well as different zoning patterns in LCT-B quartz (Figs. 2, 6a). We interpret the Population 1 sanidine as recording a single recharge event, while the Population 2 sanidine record multiple small events. The same is implied from the variable zoning patterns recorded in LCT-B quartz. The unzoned Population 3 sanidine have orthoclase and Ba contents comparable to both the core and rim compositions of the Population 1 sanidine (Fig. 3). One possibility is that the Ba-poor Population 3 crystals were derived from the magma in the system that did not mix with the recharge magma, while the Ba-rich Population 3 crystals were derived from the recharge magma itself, as dynamic simulations of mush systems suggest individual crystals see dramatically different *P–T–t* histories during a rejuvenation event depending on their location (Wallace and Bergantz 2002; Bergantz et al. 2017; Schleicher and Bergantz 2017). Alternatively, the high-Ba Population 3 sanidine may have crystallized in a homogenized melt composition after mixing and shortly before or concurrent with the explosive eruption of the LCT-B (e.g., Streck 2008 and references within). Overall, we interpret the presence of multiple sanidine phenocryst populations and variable zoning patterns of quartz as sampling both the resident (pre-eruptive) LCT-B magma and the rejuvenation material itself.

Phenocryst record in summary

In summary, we interpret the compositions and textures of the LCT-B feldspar and quartz phenocrysts as suggesting a composite history for the LCT-B pre-eruptive system: (1) crystallization of quartz cores and Population 1 and 2 sanidine cores in a mush stored at 80–150 MPa (which possibly experienced more than one rejuvenation event indicated by complexly zoned crystal interiors), (2) rejuvenation of a more juvenile silicic magma into this mush that provides the impetus for the resorption of the quartz and Population 1 and 2 sanidine cores and enriches the melt in Ba, Sr, Ti, and (3) decompression-related growth of quartz and Population 1 and 2 sanidine rims which incorporate the higher abundance magmaphile elements from the rejuvenation material.

Likely eruption trigger

In order to trigger an eruption, sufficient overpressure needs to be achieved such that dike propagation can occur (e.g., Jellinek and DePaolo 2003; Degruyter et al. 2016). The simplest explanation to produce the necessary overpressure, as suggested by the phenocryst record, is the addition of material during the rejuvenation event. In this scenario, the resident LCT-B reservoir and surrounding crust are unable to accommodate the additional volume of rejuvenation material. The recharge of magma, if it occurs rapidly and for a prolonged duration, has been shown in thermomechanical models to be capable of producing the necessary overpressures to trigger an eruption (e.g., 0.05 km^3 $year^{-1}$ for 60 years; Degruyter et al. 2016). It is worth noting that, the ability to trigger an eruption in these models is heavily dependent on the degree of crystallinity of the magmatic system prior to rejuvenation, where lower crystallinity magmas are more mobile and therefore more likely to ascend, compared to higher crystallinity magmas (e.g., Lejeune and Richet 1995; Gualda et al. 2012; Degruyter et al. 2016; Bergantz et al. 2017). If we rely on the extent of crystallization predicted by rhyolite-MELTS for the LCT-B whole rock composition (Fig. 7), the system was ~ 15% crystalline at the temperatures and pressures predicted by phenocryst rim thermobarometry (relevant to the syn- or post-rejuvenation state), far above the predicted crystal content of "rheological lock-up" (i.e., 40–60 vol% crystalline; Huber et al. 2012). This suggests LCT-B magma may have been primed for remobilization and ascent following the rejuvenation (e.g., Bachmann and Bergantz 2003).

During decompression, it is likely that the rapid crystallization of LCT-B phenocryst rims leads to significant volatile release (i.e., second boiling), a process which could have contributed to the overpressure required for an explosive eruption and/or increased the magmatic ascent rates following rejuvenation. The volatile contents constrained by quartz-hosted melt inclusions (3.4 wt% H_2O, Gansecki 1998; 4 wt% H_2O, Befus et al. 2018) combined with the rim crystallization pressures, constrained by various geobarometers (80–150 MPa; Gualda et al. 2012; Gualda and Ghiorso 2014) predict LCT-B would have experienced a significant positive volume change (5–15 vol%) associated with vapor exsolution (Sisson and Bacon 1999). Rhyolite-MELTS predicts that LCT-B magma was volatile-saturated at the recorded rim temperatures, consistent with this possible scenario (e.g., Degruyter et al. 2016; Fig. 7).

Using the timescales constrained by the feldspar and quartz growth (years or less) and those constrained by trace element diffusion (less than a few decades), we can calculate an ascent rate for the LCT-B magma. If we use a conservative timescale of 20 years, this equates to an ascent rate of ~ 60–450 m yr^{-1}, which is relatively slow, not only for the nature of an explosive eruption but also when comparing to other published rates acquired from diffusion chronometry. For example, Gualda and Sutton (2016) calculated decompression occurred within 1 year or less leading to the eruption of the Bishop Tuff and Kelley and Wartho (2000) obtained timescales of hours to days for kimberlite ascent from mantle to surface. Instead, ascent rates calculated for LCT-B are more comparable with ascent rates acquired from U-series disequilibria ranging from 10 to 1000 m yr^{-1} (Stracke et al. 2006; Rubin et al. 2005). Alternatively, our shorter timescales from crystal growth rate estimates suggest ascent rates of ~ 480–7700 m yr^{-1}. This faster ascent rate is more comparable to those calculated for other explosive, large silicic eruptions and may represent ascent rates aided by the additional driving force of second boiling.

In summary, we argue that rejuvenation of the magmatic reservoir is the most likely eruption trigger for the LCT-B eruption, as it is the simplest process recorded in the feldspar and quartz phenocryst textures and compositions that could also produce the overpressure to drive the ascent of magma. Our calculations suggest second boiling during the subsequent ascent and crystallization of the LCT-B magma may have supplied an additional driving force for the explosive nature of the eruption and promoted faster ascent rates following rejuvenation.

Comparison to other caldera-forming eruptions

When examining petrologic studies on other caldera-forming eruptions, Flaherty et al. (2018), Sigurdsson et al. (1985) and Morgan et al. (2006) investigated zoned phenocrysts to invoke magma injection and subsequent mixing during the few centuries to years prior to the Minoan eruption of Santorini volcano and the AD 79 eruption of Vesuvius. Alternatively, Gualda and Sutton (2016) and Allan et al. (2013) both find no evidence for rejuvenation as a triggering mechanism for the eruption of the Bishop Tuff at Long Valley and the Oruanui eruption at Taupo Volcano, but rather invoke decompression as the driver for crystal growth, and on relatively short timescales too [1 year (Gualda and Sutton 2016) and $\leq$1600 years (Allan et al. 2013)]. Our analyses of LCT-B suggest a mixture of these two sets of studies, with timescales on the short end of those invoking rejuvenation to eruption timescales despite its significant size, and on the long end of those simply invoking decompression-related crystal growth. It should be noted, however, the prior comparable diffusion chronometry studies commonly examine only a single element-mineral pair to calculate a timescale (e.g., Wilson et al. 2006; Morgan et al. 2006; Wark et al. 2007; Allan et al. 2013; Chamberlain et al. 2014; Gualda and Sutton 2016; Pamukcu et al. 2016; Rubin et al. 2017; Flaherty et al. 2018), rather than multiple elements with different diffusivities, and thus may overlook profiles that are a product

of crystal growth in an evolving magma composition rather than solely diffusion. Therefore, these timescales should be viewed as maxima. When the LCT-B Ba in sanidine concentration profiles are treated as resulting from diffusion alone, they yield timescales of thousands of years, whereas looking at elements with multiple diffusivities as done here reveals a more complex story dictated by sanidine growth and timescales of decades or less.

Magmatic recharge or rejuvenation appears to be a common precursor to these large volcanic eruptions and LCT-B appears to represent another such example. Continuing to conduct similar studies on other large eruptions in the Yellowstone system, as well as other caldera-forming eruptions worldwide, is critical for building up statistically robust datasets of the specific triggering mechanism, in addition to characteristic trigger-to-eruption timescales for these eruptions. For example, there is some suggestion that deep long-period earthquakes may be associated with fluid exsolution of magmatic systems (e.g., Nichols et al. 2011; Sisson et al. 2017; Cassidy et al. 2016, 2017), and further work to substantiate this link, in concert with studies such as this, could facilitate mitigating hazard for future caldera-forming eruptions. Such datasets can then have the potential to inform our approaches to volcano monitoring, and our hazard assessments of active silicic volcanic systems.

Summary and conclusions

Our petrologic investigation of bulk fallout ash and phenocryst rims from Yellowstone's most recent supereruption (ca. 631 ka) reveals at least one rejuvenation event in which more juvenile magma was introduced to a reservoir of preexisting mush, leading to decompression and phenocryst rim growth within a couple of decades or less prior to the eruption, similar to other studies of caldera systems (e.g., Morgan et al. 2006; Druitt et al. 2012; Saunders et al. 2012). We interpret multiple zoning patterns and populations of LCT-B sanidine and quartz as the result of mixing the resident LCT-B magma with rejuvenation material itself. Although it is difficult to unambiguously identify the mechanism that generated the overpressure to drive the eruption, this work points toward a rejuvenation event producing the initial overpressure, and subsequent second boiling during the ascent and crystallization of the LCT-B magma likely supplying additional overpressure and faster ascent rates to produce the extremely explosive nature of the eruption. Thus, this study informs the timing and triggering mechanism of a supereruption at Yellowstone Caldera, and motivates continued study of the physical mechanism capable of mobilizing > 1000 km^3 of material in such a short amount of time.

Acknowledgements Thanks to the National Park Service for the scientific permit (YELL-2015-SCI-6078) that made this research possible. We thank Matt Coble (Stanford-U.S. Geological Survey SHRIMP-RG lab) for assistance during CL imaging as well as Axel Wittman and Maitrayee Bose (Arizona State University) for assistance with the electron microprobe and NanoSIMS analyses respectively. Thank you to Mark Ghiorso for helpful discussions regarding rhyolite-MELTS modeling. The authors would also like to thank Tim Druitt and Mary Reid for their thoughtful and constructive comments that improved this manuscript. This study was supported by an NSF CAREER Grant EAR-1654584 to Till.

References

Allan ASR, Wilson CJN, Millet MA, Wysoczanski RJ (2012) The invisible hand: tectonic triggering and modulation of a rhyolitic supereruption. Geology 40:563–566. https://doi.org/10.1130/G32969.1

Allan ASR, Morgan DJ, Wilson CJN, Millet MA (2013) From mush to eruption in centuries: assembly of the super-sized Oruanui magma body. Contrib Mineral Petrol 166(1):143–164

Bachmann O, Bergantz GW (2003) Rejuvenation of the Fish Canyon magma body: a window into the evolution of large-volume silicic magma systems. Geology 31(9):789

Bachmann O, Huber C (2016) Silicic magma reservoirs in the Earth's crust. Am Mineral 101:2377–2404. https://doi.org/10.2138/am-2016-5675

Bachmann O, Deering CD, Lipman PW, Plummer C (2014) Building zoned ignimbrites by recycling silicic cumulates: insight from the 1,000 km^3 Carpenter Ridge Tuff, CO. Contrib Mineral Petrol 167:1–13. https://doi.org/10.1007/s00410-014-1025-3

Befus KS, Bruyere RH, Manga M (2018) Lava Creek Tuff Love. Goldschmidt Abstracts 162

Bergantz GW, Schleicher JM, Burgisser A (2017) On the kinematics and dynamics of crystal-rich systems. J Geophys Res Solid Earth 122(8):6131–6159

Bindeman IN, Valley JW (2001) Low-d18O rhyolites from Yellowstone: magmatic evolution based on analyses of zircon and individual phenocrysts. J Petrol 42:1491–1517

Blundy JD, Wood BJ (1991) Crystal-chemical controls on the partitioning of Sr and Ba between plagioclase feldspar, silicate melts, and hydrothermal solutions. Geochem Cosmochim Acta 55:193–209

Blundy J, Cashman K, Humphreys M (2006) Magma heating by decompression-driven crystallization beneath andesite volcanoes. Nat Lett 443:76–80. https://doi.org/10.1038/nature05100

Blundy J, Cashman KV, Rust A, Witham F (2010) A case for CO_2-rich arc magmas. Earth Planet Sci Lett 290:289–301. https://doi.org/10.1016/j.epsl.2009.12.013

Cabaniss HE, Gregg PM, Grosfils EB (2018) The role of tectonic stress in triggering large silicic caldera eruptions. Geophys Res Lett 45:3889–3895. https://doi.org/10.1029/2018GL077393

Calzolaio M, Arzilli F, Carroll MR (2010) Growth rate of alkali feldspars in decompression-induced crystallization experiments in a trachytic melt of the Phlegraean Fields (Napoli, Italy). Eur J Mineral 22:485–493. https://doi.org/10.1127/0935-1221/2010/0022-2012

Cashman KV, Sparks RSJ (2013) How volcanoes work: a 25 year perspective. GSA Bull 125:664–690. https://doi.org/10.1130/b30720.1

Cassidy M, Castro JM, Helo C, Troll VR, Deegan FM, Muir D, Mueller SP (2016) Volatile dilution during magma injections and implications for volcano explosivity. Geology 44(12):1027–1030

Cassidy M, Castro J, Helo C, Ebmeier S, Watt S (2017) Combining experimental petrology with InSAR deformation constraints on

the magmatic system prior to recent eruptions at Kelud volcano, Indonesia. EGU Gen Assembly Conf Abstr 19:9156
Chamberlain KJ, Morgan DJ, Wilson CJN (2014) Timescales of mixing and mobilisation in the Bishop Tuff magma body: perspectives from diffusion chronometry. Contrib Mineral Petrol 168:1–24. https://doi.org/10.1007/s00410-014-1034-2
Cherniak DJ (1996) Strontium diffusion in sanidine and albite, and general comments on strontium diffusion in alkali feldspars. Geochim Cosmochim Acta 60:5037–5043. https://doi.org/10.1016/S0016-7037(96)00293-1
Cherniak DJ (2002) Ba diffusion in feldspar. Geochim Cosmochim Acta 66:1641–1650. https://doi.org/10.1016/S0016-7037(01)00866-3
Cherniak DJ, Watson EB, Wark DA (2007) Ti diffusion in quartz. Chem Geol 236:65–74. https://doi.org/10.1016/j.chemgeo.2006.09.001
Christiansen RL (2001) The quaternary and pliocene Yellowstone Plateau Volcanic Field of Wyoming, Idaho, and Montana. USGS Professional Papers. No. 729-G
Costa F, Morgan D, Dosseto A, Turner S, Van Orman J (2011) Time constraints from chemical equilibration in magmatic crystals. Timescales of magmatic processes: from core to atmosphere. Wiley, Chichester, pp 125–159
Couch S, Harford CL, Sparks RSJ, Carroll MR (2003) Experimental constraints on the conditions of formation of highly calcic plagioclase microlites at the Soufriere Hills Volcano, Montserrat. J Petrol 44:1455–1475. https://doi.org/10.1093/petrology/44.8.1455
Degruyter W, Huber C, Bachmann O et al (2016) Magma reservoir response to transient recharge events: the case of Santorini volcano (Greece). Geology 44:23–26. https://doi.org/10.1130/G37333.1
Druitt TH, Costa F, Deloule E, Dungan M, Scaillet B (2012) Decadal to monthly timescales of magma transfer and reservoir growth at a caldera volcano. Nature 482:77–80. https://doi.org/10.1038/nature10706
Eaton GP, Christiansen RL, Iyer HM, Pitt AM, Mabey DR, Blank HR, Zietz I, Gettings ME (1975) Magma Beneath Yellowstone. Science 188:787–796
Farrell J, Smith R, Husen S, Diehl T (2014) Tomography from 26 years of seismicicty revealing that the spatial extent of the Yellowstone crustal reservoir extends well beyond the Yellowstone caldera. Geophys Res Lett 41:3068–3073. https://doi.org/10.1002/2014GL059588
Fenn PM (1977) The nucleation and growth of alkali feldspars from hydrous melts. Can Mineral 15:135–161
Flaherty T, Druitt TH, Tuffen MD et al (2018) Multiple timescale constraints for high-flux magma chamber assembly prior to the Late Bronze Age eruption of Santorini (Greece). Contrib Mineral Petrol 173:75. https://doi.org/10.1007/s00410-018-1490-1
Gansecki CA (1998) $^{40}Ar/^{39}Ar$ geochronology and pre-eruptive geochemistry of the Yellowstone Plateau volcanic field rhyolites. Unpublished doctoral dissertation, Stanford University, p 212
Gansecki CA, Mahood GA, McWilliams M (1998) New ages for the climactic eruptions at Yellowstone: single-crystal $^{40}Ar/^{39}Ar$ dating identifies contamination. Geology 26(343):346. https://doi.org/10.1130/0091-7613
Gardner JE, Befus KS, Gualda GAR, Ghiorso MS (2014) Experimental constraints on rhyolite-MELTS and the Late Bishop Tuff magma body. Contrib Mineral Petrol 168:1–14. https://doi.org/10.1007/s00410-014-1051-1
Ghiorso MS, Gualda GAR (2015) An H_2O–CO_2 mixed fluid saturation model compatible with rhyolite-MELTS. Contrib Mineral Petrol 169:1–30. https://doi.org/10.1007/s00410-015-1141-8
Ginibre C, Wörner G, Kronz A (2004) Structure and dynamics of the Laacher See magma chamber (Eifel, Germany) from major and trace element zoning in sanidine: a cathodoluminescence and electron microprobe study. J Petrol 45:2197–2223. https://doi.org/10.1093/petrology/egh053
Gregg PM, Gros EB, De Silva SL (2015) Catastrophic caldera-forming eruptions II: the subordinate role of magma buoyancy as an eruption trigger. J Volcanol 305:100–113. https://doi.org/10.1016/j.jvolgeores.2015.09.022
Gualda GA, Ghiorso MS (2014) Phase-equilibrium geobarometers for silicic rocks based on rhyolite-MELTS. Part 1: Principles, procedures, and evaluation of the method. Contrib Mineral Petrol 168(1):1033
Gualda GAR, Sutton SR (2016) The year leading to a supereruption. PLoS One 11:1–18. https://doi.org/10.1371/journal.pone.0159200
Gualda GAR, Ghiorso MS, Lemons RV, Carley TL (2012) Rhyolite-MELTS: a modified calibration of MELTS optimized for silica-rich, fluid-bearing magmatic systems. J Petrol 53:875–890. https://doi.org/10.1093/petrology/egr080
Guo J, Green TH (1989) Barium partitioning between alkali feldspar and silicate liquid at high temperature and pressure. Contrib Mineral Petrol 102(3):328–335
Hawkesworth C, George R, Turner S, Zellmer G (2004) Time scales of magmatic processes. Earth Planet Sci Lett 218:1–16. https://doi.org/10.1016/S0012-821X(03)00634-4
Hayden LA, Watson EB (2007) Rutile saturation in hydrous siliceous melts and its bearing on Ti-thermometry of quartz and zircon. Earth Planet Sci Lett 258:561–568. https://doi.org/10.1016/j.epsl.2007.04.020
Hildreth W (1981) Gradients in silicic magma chambers: implications for lithospheric magmatism. J Geophys Res Solid Earth 86(B11):10153–10192
Hildreth W, Christiansen RL, O'Neil JR (1984) Catastrophic isotopic modification of rhyolitic magma at times of caldera subsidence, Yellowstone Plateau volcanic field. J Geophys Res Solid Earth 89(B10):8339–8369
Hildreth W, Halliday AN, Robert L (1991) Isotopic and chemical evidence concerning the genesis and contamination of basaltic and rhyolitic magma beneath the Yellowstone Plateau Volcanic Field. J Petrol 32:63–138
Huang R, Audétat A (2012) The titanium-in-quartz (TitaniQ) thermobarometer: a critical examination and re-calibration. Geochim Cosmochim Acta 84:75–89. https://doi.org/10.1016/j.gca.2012.01.009
Huber C, Bachmann O, Dufek J (2012) Crystal-poor versus crystal-rich ignimbrites: a competition between stirring and reactivation. Geology 40:115–118. https://doi.org/10.1130/G32425.1
Humphreys MCS, Edmonds M, Klöcking MS (2016) The validity of plagioclase-melt geothermometry for degassing-driven magma crystallisation. Am Mineral 101:769–779
Iacovino K (2015) Linking subsurface to surface degassing at active volcanoes: a thermodynamic model with applications to Erebus volcano. Earth Planet Sci Lett 431(59):74. https://doi.org/10.1016/j.epsl.2015.09.016
Icenhower J, London D (1996) Experimental partitioning of Rb, Cs, Sr, and Ba between alkali feldspar and peraluminous melt. Am Mineral 81:719–734. https://doi.org/10.2138/am-1996-5-619
Jellinek AM, DePaolo DJ (2003) A model for the origin of large silicic magma chambers: precursors of caldera-forming eruptions. Bull Volcanol 65:363–381. https://doi.org/10.1007/s00445-003-0277-y
Jicha BR, Singer BS, Sobol P (2016) Re-evaluation of the ages of 40 Ar/39 Ar sanidine standards and supereruptions in the western US using a Noblesse multi-collector mass spectrometer. Chem Geol 431:54–66
Kelley SP, Wartho JA (2000) Rapid kimberlite ascent and the significance of Ar–Ar ages in xenolith phlogopites. Science 289(5479):609–611
Leeman W, Vicenzi E, Macrae C et al (2008) Systematics of cathodoluminescence and trace element compositional zoning in

natural quartz from volcanic rocks: Ti mapping in quartz. Microsc Microanal 18:1322–1341. https://doi.org/10.1017/S1431927608088995

Leeman WP, MacRae CM, Wilson NC, Torpy A, Lee CT, Student JJ, Thomas JB, Vicenzi EP (2012) A study of cathodoluminescence and trace element compositional zoning in natural quartz from volcanic rocks: mapping titanium content in quartz. Microsc Microanal 18(6):1322–1341

Lejeune AM, Richet P (1995) Rheology of crystal-bearing silicate melts: an experimental study at high viscosities. J Geophys Res Solid Earth 100(B3):4215–4229

Long PE (1978) Experimental determination of partition coefficients for Rb, Sr, and Ba between alkali feldspar and silicate liquid. Geochim Cosmochim Acta 42:833–846

Mark DF, Renne PR, Dymock RC, Smith VC, Simon JI, Morgan LE, Pearce NJ (2017) High-precision $^{40}Ar/^{39}Ar$ dating of Pleistocene tuffs and temporal anchoring of the Matuyama-Brunhes boundary. Quat Geochron 39:1–23

Matthews NE, Huber C, Pyle DM, Smith VC (2012) Timescales of magma recharge and reactivation of large silicic systems from Ti diffusion in quartz. J Petrol 53:1385–1416. https://doi.org/10.1093/petrology/egs020

Matthews N, Vazquez J, Calvert A (2015) Age of the Lava Creek supereruption and magma chamber assembly at Yellowstone based on $^{40}Ar/^{39}Ar$ and U–Pb dating of sanidine and zircon crystals. Geochem Geophys Geosyst 16:1–21. https://doi.org/10.1002/2015GC005881

Morgan DJ, Blake S, Rogers NM et al (2006) Magma chamber recharge at Vesuvius in the century prior to the eruption of A.D. 79. Geology 34:845–848. https://doi.org/10.1130/G22604.1

Müller A, Wiedenbeck M, van den Kerkhof AM et al (2003) Trace elements in quartz—a combined electron microprobe, secondary ion mass spectrometry, laser-ablation ICP-MS, and cathodoluminescence study. Eur J Mineral 15:747–763. https://doi.org/10.1127/09351221/2003/0015-0747

Nichols ML, Malone SD, Moran SC, Thelen WA, Vidale JE (2011) Deep long-period earthquakes beneath Washington and Oregon volcanoes. J Volcanol Geotherm Res 200(3–4):116–128

Oppenheimer C, Moretti R, Kyle PR et al (2011) Mantle to surface degassing of alkalic magmas at Erebus volcano, Antarctica. Earth Planet Sci Lett 306:261–271. https://doi.org/10.1016/j.epsl.2011.04.005

Pamukcu AS, Ghiorso MS, Gualda GAR (2016) High-Ti, bright-CL rims in volcanic quartz: a result of very rapid growth. Contrib Mineral Petrol 171:1–9. https://doi.org/10.1007/s00410-016-1317-x

Putirka KD (2008) Thermometers and barometers for volcanic systems. Rev Mineral Geochem 69:61–120. https://doi.org/10.2138/rmg.2008.69.3

Ren M (2004) Partitioning of Sr, Ba, Rb, Y and LREE between alkali feldspar and peraluminous silicic magma. Am Mineral 89(8–9):1290–1303

Rubin KH, van der Zander I, Smith MC, Bergmanis EC (2005) Minimum speed limit for ocean ridge magmatism from ^{210}Pb–^{226}Ra–^{230}Th disequilibria. Nature 437:534–538

Rubin AE, Cooper KM, Till CB et al (2017) Rapid cooling and cold storage in a silicic magma reservoir recorded in individual crystals. Science 356:1154–1156. https://doi.org/10.1126/science.aam8720

Saunders K, Blundy J, Dohmen R, Cashman K (2012) Linking petrology and seismology at an active volcano. Science 336(6084):1023–1027

Schleicher JM, Bergantz GW (2017) The mechanics and temporal evolution of an open-system magmatic intrusion into a crystal-rich magma. J Petrol 58(6):1059–1072

Schneider CA, Rasband WS, Eliceiri KW (2012) NIH Image to ImageJ: 25 years of image analysis. Nat Methods 9(7):671–675

Sigurdsson H, Carey S, Cornell W, Pescatore T (1985) The eruption of Vesuvius in A.D. 79. Natl Geogr Res 1(3):332–387

Sisson TW, Bacon CR (1999) Gas-driven filter pressing in magmas. Geology 27:613–616. https://doi.org/10.1130/0091-7613(1999)027%3c0613:GDFPIM%3e2.3.CO

Sisson T, Power J, Haney M (2017) The deep-crustal roots of arc stratovolcanoes illuminated by long-period seismicity caused by degassing and fluid-enhanced wallrock embrittlement. IAVCEI General Assembly Submission 920

Smith RB, Braile LW (1994) The Yellowstone hotspot. J Volcanol Geotherm Res 61:121–187. https://doi.org/10.1016/0377-0273(94)90002-7

Smith J, Brown WL (1988) Feldspar minerals: crystal structures, physical, chemical and microtextural properties. Springer, Berlin, p 828

Smith RB, Jordan M, Steinberger B et al (2009) Geodynamics of the Yellowstone hotspot and mantle plume: seismic and GPS imaging, kinematics, and mantle flow. J Volcanol Geotherm Res 188:26–56. https://doi.org/10.1016/j.jvolgeores.2009.08.020

Sparks S (2005) Super-eruptions: global effects and future threats, report of a Geological Society of London Working Group. Geological Society, London

Stelten ME, Cooper KM, Vazquez JA et al (2013) Magma mixing and the generation of isotopically juvenile silicic magma at Yellowstone caldera inferred from coupling 238 U–230 Th ages with trace elements and Hf and O isotopes in zircon and Pb isotopes in sanidine. Contrib Mineral Petrol 166(2):587–613. https://doi.org/10.1007/s00410-013-0893-2

Stelten ME, Cooper KM, Vazquez JA et al (2015) Mechanisms and timescales of generating eruptible rhyolitic magmas at Yellowstone Caldera from Zircon and sanidine geochronology and geochemistry. J Petrol 56:1607–1642. https://doi.org/10.1093/petrology/egv047

Stelten ME, Cooper KM, Wimpenny JB et al (2017) The role of mantle-derived magmas in the isotopic evolution of Yellowstone's magmatic system. Geochem Geophys Geosyst 18:1350–1365. https://doi.org/10.1002/2016GC006664

Stracke A, Bourdon B, McKenzie D (2006) Melt extraction in the Earth's mantle: constraints from U-Th–Pa–Ra studies in oceanic basalts. Earth Planet Sci Lett 244:97–112

Streck MJ (2008) Mineral textures and zoning as evidence for open system processes. Rev Mineral Geochem 69:595–622. https://doi.org/10.2138/rmg.2008.69.15

Swanson SE (1974) Phase equilibria and crystal growth in granodioritic and related systems with $H_2O + CO_2$. Ph.D. thesis, Stanford University

Swanson SE (1977) Relation of nucleation and crystal-growth rate to the development of granitic textures. Am Mineral 62:966–978

Thomas JB, Watson EB, Spear FS et al (2010) TitaniQ under pressure: the effect of pressure and temperature on the solubility of Ti in quartz. Contrib Mineral Petrol 160:743–759. https://doi.org/10.1007/s00410-010-0505-3

Till CB, Vazquez JA, Boyce JW (2015) Months between rejuvenation and volcanic eruption at Yellowstone caldera, Wyoming. Geology. https://doi.org/10.1130/g36862

Turner S, Costa F (2007) Measuring timescales of magmatic evolution. Elements 3:267–272

Vazquez JA, Kyriazis SF, Reid MR et al (2009) Thermochemical evolution of young rhyolites at Yellowstone: evidence for a cooling but periodically replenished postcaldera magma reservoir. J Volcanol Geotherm Res 188:186–196. https://doi.org/10.1016/j.jvolgeores.2008.11.030

Wallace G, Bergantz GW (2002) Wavelet-based correlation (WBC) of zoned crystal populations and magma mixing. Earth Planet Sci Lett 202:133–145

Wallace PJ, Anderson AT et al (1995) Quantification of pre-eruptive exsolved gas contents in silicic magmas. Nature 377:612–616

Wark DA, Watson EB (2006) TitaniQ: a titanium-in-quartz geothermometer. Contrib Mineral Petrol 152:743–754. https://doi.org/10.1007/s00410-006-0132-1

Wark DA, Hildreth W, Spear FS et al (2007) Pre-eruption recharge of the Bishop magma system. Geology 35:235–238. https://doi.org/10.1130/G23316A.1

Watts KE, Bindeman IN, Schmitt AK (2012) Crystal scale anatomy of a dying supervolcano: an isotope and geochronology study of individual phenocrysts from voluminous rhyolites of the Yellowstone caldera. Contrib Mineral Petrol 164(1):45–67

Wilke S, Holtz F, Neave DA, Almeev R (2017) The effect of anorthite content and water on quartz-feldspar cotectic compositions in the rhyolitic system and implications for geobarometry. J Petrol 58:789–818. https://doi.org/10.1093/petrology/egx034

Wilson CJN, Blake S, Charlier BLA, Sutton AN (2006) The 26.5 ka Oruanui Eruption, Taupo Volcano, New Zealand: development, characteristics and evacuation of a large rhyolitic magma body. J Petrol 47:35–69. https://doi.org/10.1093/petrology/egi066

Wilson CJN, Stelten ME, Lowenstern JB (2018) Contrasting perspectives on the Lava Creek Tuff eruption, Yellowstone, from new U-Pb and $^{40}Ar/^{39}Ar$ age determinations. Bull Volcanol 80(6):53

Wotzlaw JF, Bindeman IN, Stern RA et al (2015) Rapid heterogeneous assembly of multiple magma reservoirs prior to Yellowstone supereruptions. Sci Rep 5:1–10. https://doi.org/10.1038/srep14026

Zellmer GF, Clavero JE (2006) Using trace element correlation patterns to decipher a sanidine crystal growth chronology: an example from Taapaca volcano, Central Andes. J Volcanol Geotherm Res 156:291–301. https://doi.org/10.1016/j.jvolgeores.2006.03.004

Zhang Y (2008) Geochemical kinetics. Princeton University Press, Princeton, p 656